Batteries & Supercaps

Research Article
doi.org/10.1002/batt.202400420

Chemistry Europe
European Chemical Societies Publishing

www.batteries-supercaps.org

Effect of Chloride Ions on the Electrochemical Performance of Magnesium Metal-Organic-Frameworks-Based Semi-Solid Electrolytes

Mohamed M. Elnagar,[a] Hagar K. Hassan,*[a, b, c] Ludwig A. Kibler,[a] and Timo Jacob*[a, b, c]

The majority of research on magnesium (Mg) electrolytes has focused on enhancing reversible Mg deposition, often employing chloride-containing electrolytes. However, there is a notable gap in the literature regarding the influence of chloride ions in semi-solid Mg electrolytes. In this study, we systematically explore the impact of chloride ions on Mg deposition/dissolution on a copper (Cu) anode using a semi-solid electrolyte composed of Mg-based mixed metal-organic frameworks, $MgCl_2$ and $Mg[TFSI]_2$. We separate the Mg deposition/dissolution process from changes in the anode's surface morphology In this respect, the morphological and compositional transformations in the electrolyte and electrode following galvanostatic cycling are meticulously investigated. Initial potential cycling reveals the feasibility of Mg deposition/dissolution on Cu electrodes, albeit with reduced reversibility in subsequent cycles. Extending the upper potential limit to 4.0 V *vs.* Mg/Mg^{2+} enhances Mg dissolution, attributed to chloride ions facilitating Cu surface dissolution. Our findings provide insights into optimizing semi-solid electrolytes for advanced Magnesium battery technologies.

1. Introduction

In recent years, research has increasingly shifted towards rechargeable multivalent-ion batteries, with magnesium-ion batteries standing out as a compelling alternative to lithium-ion technology.[1,2] In this context, Mg offers several advantages, including abundant natural reserves, low cost (approximately 24 times cheaper than Li), high safety, a high theoretical energy density (3832 Ah L^{-1} *vs.* 2062 Ah L^{-1} for Li), and a low electrode potential ($E^{\circ} = -2.37$ V *vs.* SHE), making it an extremely appealing option for large-scale battery applications.[1,3–6] However, one of the primary challenges in realizing the practical application of Mg-ion batteries lies in the development of suitable electrolytes. These electrolytes must possess several key characteristics, including favorable ionic conductivity, non-corrosiveness, efficient reversibility in the deposition and stripping of Mg^{2+} ions, a wide electrochemical stability window, and compatibility with various positive and negative electrode materials.[7–10]

In the pursuit of suitable electrolytes for Mg-ion batteries, various non-aqueous liquid electrolyte systems composed of complex salts and organic solvents have been investigated.[8–12] For example, Mg-chloride complex electrolytes, which combine an Mg-containing Lewis base (*e.g.* Grignard reagents and $MgCl_2$) with a Lewis acid (*e.g.* $AlCl_3$ and $AlPh_3$) exhibit high Coulombic efficiencies for magnesium batteries.[12–16] These electrolytes feature active species characterized by Mg–Cl coordination moieties. Several studies have demonstrated that chloride ions facilitate both the deposition and the dissolution of Mg and prevent the formation of passivation layers.[17–22] In this respect, chloride ions inhibit Mg surface passivation by forming adsorbed Cl^- and/or $MgCl_2$ on the Mg surface through a dynamic competition with adventitious H_2O impurities in the double layer.[21,23] However, the presence of chloride (or other highly electronegative anions) contributes to the corrosive nature of these electrolytes. In particular, chloride ions would corrode the battery components when the potential exceeds 2.5 V, thus affecting the electrochemical window and lifetime of the battery.[24–26] Boron-based electrolytes have been proposed as chloride-free alternatives for Mg batteries due to their extended voltage window.[27–31] Despite being anodically stable, those systems still suffer from relatively high cost, poor reproducibility, and non-dendrite short-circuiting.[27,28,32,33] Moreover, electrolytes based on $Mg(PF_6)_2$ in THF, and $Mg[TFSI]_2$ in glymes, have also been reported, demonstrating significant Mg deposition/dissolution capabilities.[34–38] However, even with their ability to operate at voltages up to 3.4 V *vs.* Mg/Mg^{2+}, these electrolytes possess certain drawbacks. They are volatile, flammable, and corrosive, particularly towards commonly used current collectors and cell cases made of copper, aluminum, nickel, and stainless steel.[34–38] Instead, semi-solid-state electrolytes, typically comprising polymers or inorganic frameworks, magnesium salts, and minimal solvent contents, present

[a] M. M. Elnagar, H. K. Hassan, L. A. Kibler, T. Jacob
Institute of Electrochemistry, Ulm University, 89081 Ulm, Germany
E-mail: hagar.ibrahim@kit1.edu

[b] H. K. Hassan, T. Jacob
Helmholtz-Institute-Ulm (HIU) Electrochemical Energy Storage, 89081 Ulm, Germany.

[c] H. K. Hassan, T. Jacob
Karlsruhe Institute of Technology (KIT), P.O. Box 3640, 76021, Karlsruhe, Germany

Supporting information for this article is available on the WWW under https://doi.org/10.1002/batt.202400420

Research Article
doi.org/10.1002/batt.202400420
Chemistry Europe
European Chemical Societies Publishing

numerous advantages.[39–46] These advantages include their freestanding nature, non-volatility, enhanced safety, thermal stability, improved electrode wettability, and shape flexibility. Their capability to expand the electrochemical stability window is particularly noteworthy, which helps alleviate undesirable side reactions such as anodic corrosion and hydrogen evolution at electrode surfaces.[39–46] These characteristics position semi-solid electrolytes as promising candidates for advancing energy storage technologies and overcoming the challenges associated with conventional liquid electrolytes.

Recent endeavors have focused on developing semi-solid electrolytes based on diverse materials such as inorganic ceramics, organic polymers, metal coordination complexes, and metal-organic frameworks (MOFs).[39–46] Among these, semi-solid electrolytes based on MOFs stand out because MOFs offer a large surface area, allowing for the accommodation of a high density of charged species, which promotes efficient ion transport and increased ion conductivity, while effectively suppressing electronic contributions. Furthermore, the ordered porosity of MOFs helps control the uniformity of Mg deposition, preventing dendrite formation on the anode during charging. Additionally, various parameters such as metal center properties, pore polarity, and pore diameter can be manipulated to optimize the electrolyte performance systematically.[46–50]

In our previous work, we synthesized a mixture of Mg-based MOFs (denoted as *a*-MOF1), through the hydrothermal reaction of $Mg(NO_3)_2{\cdot}6H_2O$ and 2,2′-bipyridine-3,3′-dicarboxylic acid (bp3dca) in DMF as a solvent, as a possible semi-solid electrolyte for Mg-ion batteries.[50] Figure 1 illustrates the structure of these MOFs. The electrolyte comprises *a*-Mg(bp3dc) and α-$Mg_3(HCOO)_6$, which are mixed with $MgCl_2$ and $Mg[TFSI]_2$ in tetraglyme (G4). After the evaporation of excess G4, the semi-solid electrolyte exhibits a relatively high ionic conductivity of 38 $\mu S\,cm^{-1}$ at 30 °C, with a low solvent content of 15–20 %. Furthermore, it exhibited a highly reversible Mg^{2+} deposition/dissolution capability in a symmetric cell, Mg | 90 %*a*-MOF1–10 %($Mg[TFSI]_2 + MgCl_2$)-G4 | Mg, and an asymmetric cell, Cu | 90 %*a*-MOF1–10 %($Mg[TFSI]_2 + MgCl_2$)-G4 | Mg. In the present investigation, we demonstrate new findings on the performance of the developed semi-solid electrolyte towards the deposition (and dissolution) of Mg on a Cu anode in an asymmetric cell configuration: Cu | 90 %*a*-MOF1–10 %($Mg[TFSI]_2$

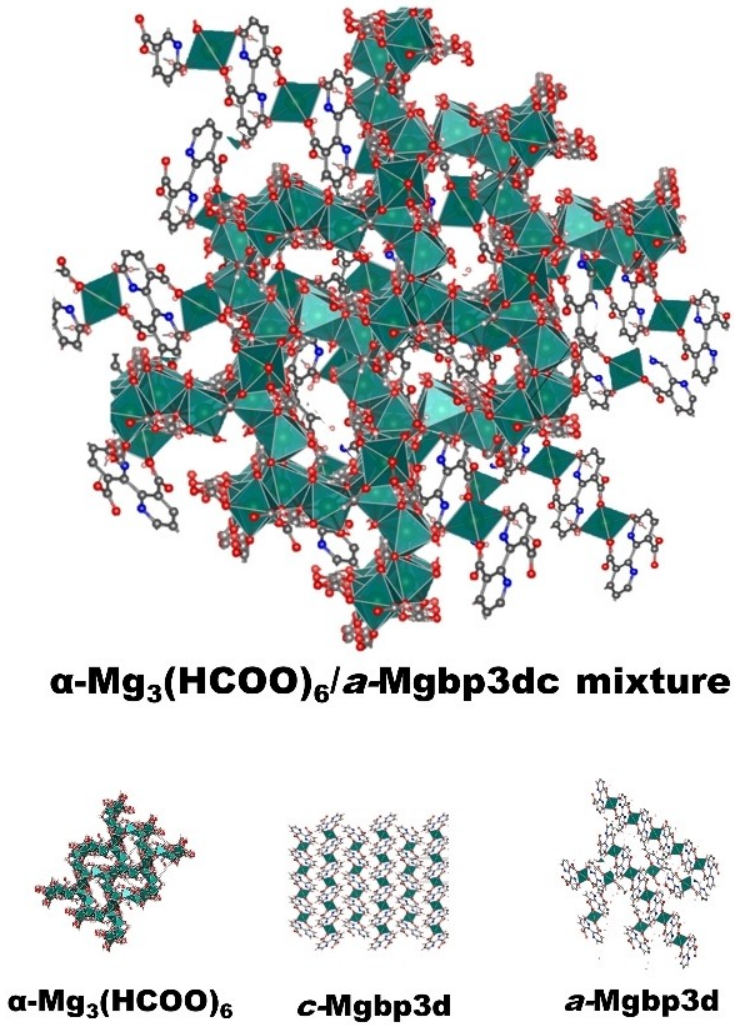

Figure 1. Molecular structure of the synthesized MOFs.

+ $MgCl_2$)-G4 | Mg. In particular, while there have been numerous studies examining the impact of chloride ions on magnesium deposition and dissolution processes,[17–22] as well as the corrosion of metal electrodes in liquid electrolytes,[24,25] the effects of chloride ions in semi-solid electrolytes remain unexplored. This study aims to bridge this research gap by systematically investigating the influence of chloride ions on anode corrosion, specifically on Cu electrodes, in semi-solid electrolytes and how this affects the Mg deposition and dissolution processes. We demonstrate through electrochemical measurements and surface characterization that the structural and compositional changes in Cu electrodes, as well as alterations in Mg deposition/dissolution processes, are unambiguously linked to the presence of chloride ions. The results indicate that the impact of chloride ions in semi-solid electrolytes is comparably significant to their effect in liquid electrolytes. Of note, in our previous study, we thoroughly optimized the electrolyte compositions with and without $MgCl_2$, demonstrating that the absence of $MgCl_2$ results in lowering the ionic conductivity by more than an order of magnitude.[50] Additionally, it is well established that in chloride-free electrolytes, the passivation layer is more pronounced. $MgCl_2$ is an essential additive to $Mg[TFSI]_2$, as it prevents Mg passivation, lowers the Mg overpotential, and enhances the reversibility.[12–23] Therefore, in this study, we focus exclusively on investigating the changes in Cu surfaces and the Mg deposition/dissolution process in the presence of $MgCl_2$.Furthermore, the stability of the electrolyte upon galvanostatic cycling at various current densities is explored.

Experimental

Material Synthesis and Solid Electrolytes Preparation

Synthesis of Mixed Metal-Organic Frameworks (MOFs)

Mixed metal organic frameworks of $Mg(bp3dc)(H_2O)_4$, $[Mg(HCOO)_3][NH_2(CH_3)_2]$ and α-$Mg_3(HCOO)_6 \cdot$DMF were synthesized as previously reported.[50] Briefly, 3.0 mmol $Mg(NO_3)_2 \cdot 6H_2O$ (99.999% trace metals basis, Sigma Aldrich) and 1.0 mmol 2,2′-bipyridine-3,3′-dicarboxylic acid (bpdca; 97%, Sigma Aldrich) were dissolved in 10 mL anhydrous N,N-dimethylformamide (DMF; 98.8%, Sigma Aldrich) solvent. The mixture was then transferred to a 50 mL Teflon-lined autoclave followed by a hydrothermal reaction at 120 °C for 72 h. The mixture was gradually cooled down to room temperature for 72 h (1.3 °C h^{-1}). The as-synthesized material (m-MOF1), was collected by centrifugation at 9000 rpm, washed at least three times with hot DMF, and dried at 70 °C.

Synthesis of a-Mg(bp3dc)-α-$Mg_3(HCOO)_6$ (a-MOF1)

A mixture of amorphous Mg(bp3dc) and α-$Mg_3(HCOO)_6$ (*a*-MOF1) was obtained by thermal activation of the as-synthesized m-MOF1 at 200 °C under a vacuum of 10 mbar for 5 h. For the preparation of solid electrolytes (SEs), *a*-MOF1 was directly stored in an Ar-filled glovebox with O_2 and H_2O levels less than 0.5 ppm.

Solid Electrolyte Preparation

The solid electrolyte was prepared in an Ar-filled glovebox by dispersing 0.2 g mL^{-1} of 90 wt% of *a*-MOF1 (α-$Mg_3(HCOO)_6$-*a*-Mgbp3dc), 5 wt% of $MgCl_2$ (Sigma Aldrich) and 5 wt% of Magnesium bis(trifluoromethanesulfonimide) ($Mg[TFSI]_2$; Sigma Aldrich) in tetraglyme (G4; ≥99%, Sigma Aldrich) under a continuous stirring for 48 h. Afterwards, the excess G4 was evaporated under vacuum and the SEs were subjected to vacuum drying at 80 °C overnight under 10 mbar. This method has been used to minimize the solvent extent in MOF-based SEs.

Cell Assembly and Electrochemical Characterizations

0.1 g of the SE powder was dispensed between two stainless steel discs into a homemade cylindrical PEEK cell with an inner diameter of 13 mm. The loaded material was then pressed at 5.2 tons for 3 min. The thickness of the formed pellets was between 0.45 to 0.58 mm. For asymmetric cell measurements, the SE pellet was sandwiched between a Mg foil (0.025 mm thickness, Ø 12 mm, Alfa Aesar) as a counter electrode and a Cu foil (0.015 mm thickness, Ø 12 mm,) as a working electrode. For electrochemical tests, the cell with the SE pellet, Mg, and Cu electrodes was hosted in a stainless steel case with an upper screw applying a force to the upper part to ensure the electrical contact and mechanical stability of the cell. The whole cell was further sealed in an aluminum case filled with Ar to avoid exposure to air. All the cells were left at OCV (1.1 V *vs.* Mg/Mg^{2+}) for 24 h before the measurements. Cyclic voltammograms, galvanostatic discharging–charging tests (GCD), and electrochemical impedance spectra (EIS) were recorded with a Biologic VMP3 multichannel potentiostat at 40 °C in a thermostatic climate chamber of a maximum deviation ±1 °C unless mentioned otherwise. All cyclic voltammograms were obtained at a scan rate of 0.5 mV s^{-1}.

Surface and Structural Characterization

Powder diffraction X-ray (PXRD) patterns were recorded on STOE Stadi P diffractometer under the following conditions – for powders: 40 kV, 40 mA, Cu–Kα radiation ($\lambda = 1.54$ Å) using the transmission mode; and for electrodes: 50 kV, 40 mA Mo–Kα1 radiation ($\lambda = 0.7093$ Å) using the diffraction mode. The powders of SE were assembled in the sample holder inside the glovebox to avoid contamination from the air. The electrodes were covered by Kapton tape inside the glovebox for further protection. X'pert PANalytical's Highscore software was used for XRD pattern analyses. The scanning electron microscope images and energy dispersive X-ray spectroscopy were carried out using Zeiss LEO 1550 VP field emission SEM (FE-SEM Carl Zeiss, Germany). X-ray photoelectron spectroscopy (XPS) measurements were conducted utilizing a Specs XPS system equipped with a Phoibos 150 energy analyzer. Monochromatic Al–Kα radiation (1486.6 eV), a take-off angle set at 45°, and a pass energy of 30 eV at the analyzer were employed for detailed spectra acquisition. Analysis of the XPS data was performed using Casa XPS software, with all spectra calibrated to the primary C-1 *s* peak (representing C–C species) at 284.8 eV. To prevent surface contamination, the samples were prepared within an Ar-filled glovebox and then transferred under an inert gas atmosphere to the sample load-lock of the XPS system.

2. Results and Discussion

The reversibility of magnesium deposition on a Cu electrode is explored with the asymmetric Cu | 90%*a*-MOF1–10%($Mg[TFSI]_2$

Research Article
doi.org/10.1002/batt.202400420
Chemistry Europe
European Chemical Societies Publishing

$+MgCl_2$)-G4|Mg cell, utilizing the semi-solid electrolyte under study. Figures S1a–e illustrate both *ex-situ* XRD and SEM-EDS analyses of the Cu electrode after Mg deposition and dissolution at $\pm 0.7\ \mu A\,cm^{-2}$, demonstrating the successful Mg deposition and dissolution processes. The corresponding chronopotentiometric curve for the Mg deposition and dissolution processes is shown in Figure S1f. The XRD pattern of the Cu electrode reveals a distinct diffraction peak observed at $2\Theta = 36°$, corresponding to the Mg (101) plane. The dissolution of magnesium is inferred from the absence of this peak (Figure S1a). Additionally, the SEM image in Figure S1b illustrates the formation of a Mg layer after Mg deposition, a finding corroborated by EDS analysis (Figure S1c). Notably, an intriguing observation emerged: pitting corrosion is evident on the Cu electrode after Mg dissolution at $-0.7\ \mu A\,cm^{-2}$, which is attributed to Cu dissolution (Figure S1d). These initial findings prompted a more in-depth exploration of the electrochemical processes occurring at the Cu surface during cycling in the 90% *a*-MOF1–10%($Mg[TFSI]_2 + MgCl_2$)-G4 electrolyte.

To distinguish Mg deposition/dissolution from other possible electrochemical processes on the Cu surface, cyclic voltammograms of Cu electrodes in the electrolyte were obtained at different potential regimes at a scan rate of $0.5\ mV\,s^{-1}$ (Figure 2a and b). In the first cycle of the cyclic voltammetry for Cu within the potential range of 0.3 V to 3.0 V *vs.* Mg/Mg^{2+}, a low-current anodic peak is observed, which is

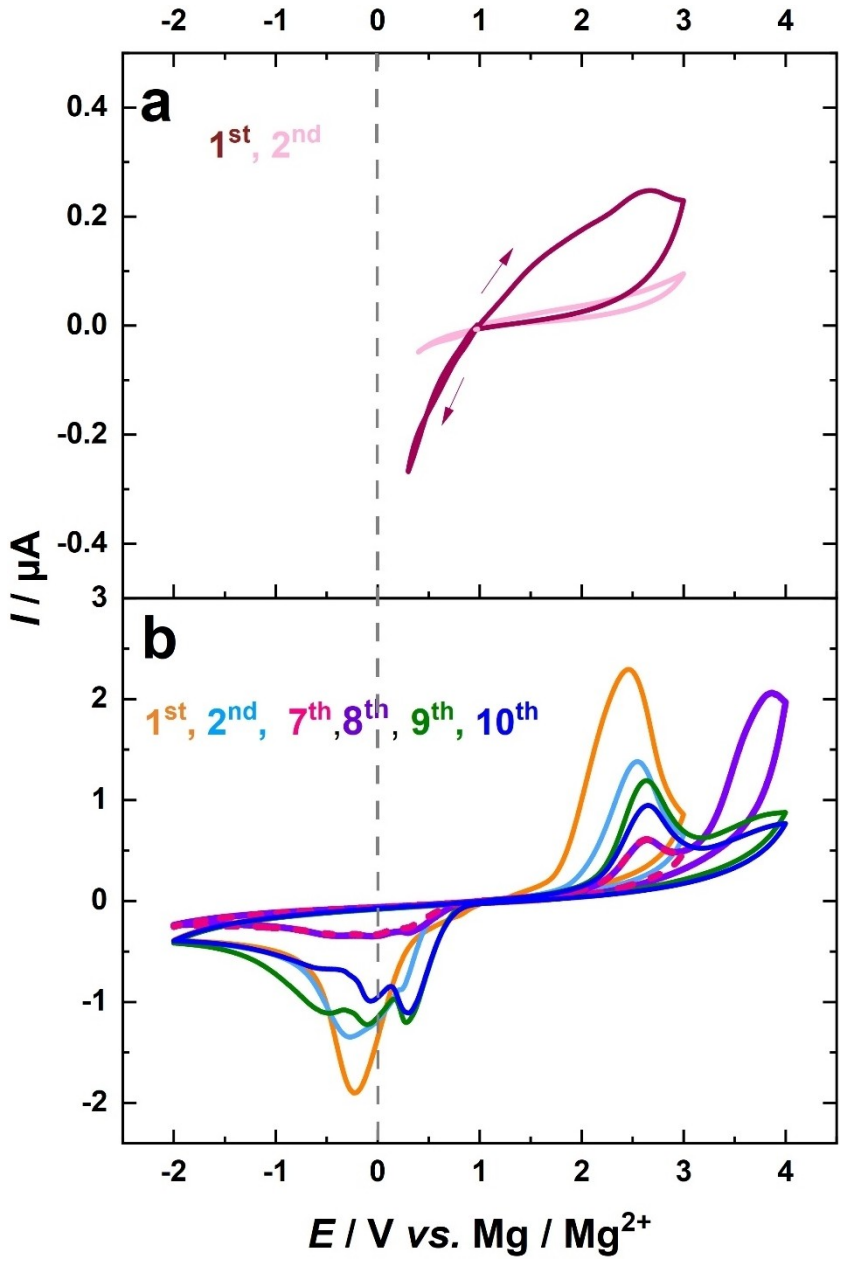

Figure 2. Cyclic voltammograms of Cu electrodes in 90%*a*-MOF1–10%($Mg[TFSI]_2 + MgCl_2$)-G4 at different potential regimes (a) from 0.3 V to 3.0 V and (b) from −2.0 up to 4.0 V *vs.* Mg/Mg^{2+} at a scan rate of $0.5\ mV\,s^{-1}$.

Research Article
doi.org/10.1002/batt.202400420
Chemistry Europe
European Chemical Societies Publishing

diminished in the subsequent cycle (Figure 2a). The appearance of the anodic peaks can be attributed to the oxidative corrosion of the Cu surface as a consequence of the presence of chloride anions. In the 2nd voltammetric cycle, the decrease in the anodic and cathodic current reveals that the adsorption process of chloride ions is irreversible. In comparison, upon lowering the potential to access the Mg deposition regime, the developed semi-solid electrolyte exhibits remarkable Mg deposition and dissolution properties within the potential window of −2.0 to 3.0 V. Peaks corresponding to Mg deposition and dissolution are observed at −0.22 V and 2.46 V *vs.* Mg/Mg^{2+}, respectively. As shown in Figure 2b, the Mg deposition/dissolution is feasible on Cu electrodes in the first cycle. However, it should be noted that the amount of charge that passed significantly decreases with cycle number (see Figures 2b, S2 and S3) owing to the limited reversibility of Mg deposition and thus the decrease in the surface centers available for further Mg deposition. Additionally, the anodic charge is higher than the cathodic charge referring to another process that takes place and overlaps with the Mg deposition. Interestingly, when the upper potential limit is extended to 4.0 V, as shown in the 8th cycle, the peaks corresponding to deposition and dissolution intensify in the subsequent 9th and 10th cycles. Furthermore, Figure S2 shows up to the 14th cycle, in which Mg deposition significantly improves following the window expansion and remains more pronounced compared to earlier cycles. The enhanced Mg dissolution results in the formation of active centers available for subsequent Mg deposition/dissolution. This is likely facilitated by the presence of chloride ions, which promote the dissolution of the Cu surface at relatively high positive potentials and, in turn, enhance the Mg dissolution process.[51,52] Furthermore, a pronounced peak arises at about 0.4 V *vs.* Mg/Mg^{2+}, which can be distinguished from Mg deposition. This might be due to Mg/Cu alloy formation that is more likely to occur at a potential more positive than 0 V *vs.* Mg/Mg^{2+}.[53] However, this could not be confirmed by *ex-situ* XRD (Figure S1a). Therefore, most probably, this is connected to the re-deposition of Cu, confirming the dissolution of Cu surfaces upon extending the potential limit to 4.0 V *vs.* Mg/Mg^{2+}.

To evaluate the durability of the electrolyte after several successive cycles, we performed an additional Mg deposition–dissolution cycle using a fresh Cu electrode in the same electrolyte (Figure 3a). Notably, the Mg deposition and dissolution behavior is comparable to that obtained in the first cycle with a fresh electrolyte (see Figures 2b and 3a). This indicates that the enhancement in the Mg deposition/dissolution upon extending the upper potential limit to 4.0 V is primarily related to changes in the Cu surface upon oxidation, rather than to changes in the electrolyte. The presence of chloride anions in the electrolyte can impact not only the surface structure of the Cu working electrode but also the Mg counter electrode, which may result in potential shifts. To ascertain that the cathodic current observed at $E > 0$ V *vs.* Mg/Mg^{2+} (Figure 2b) is attributed to Cu electrochemical processes rather than Mg deposition, the electrochemical processes within this potential regime are

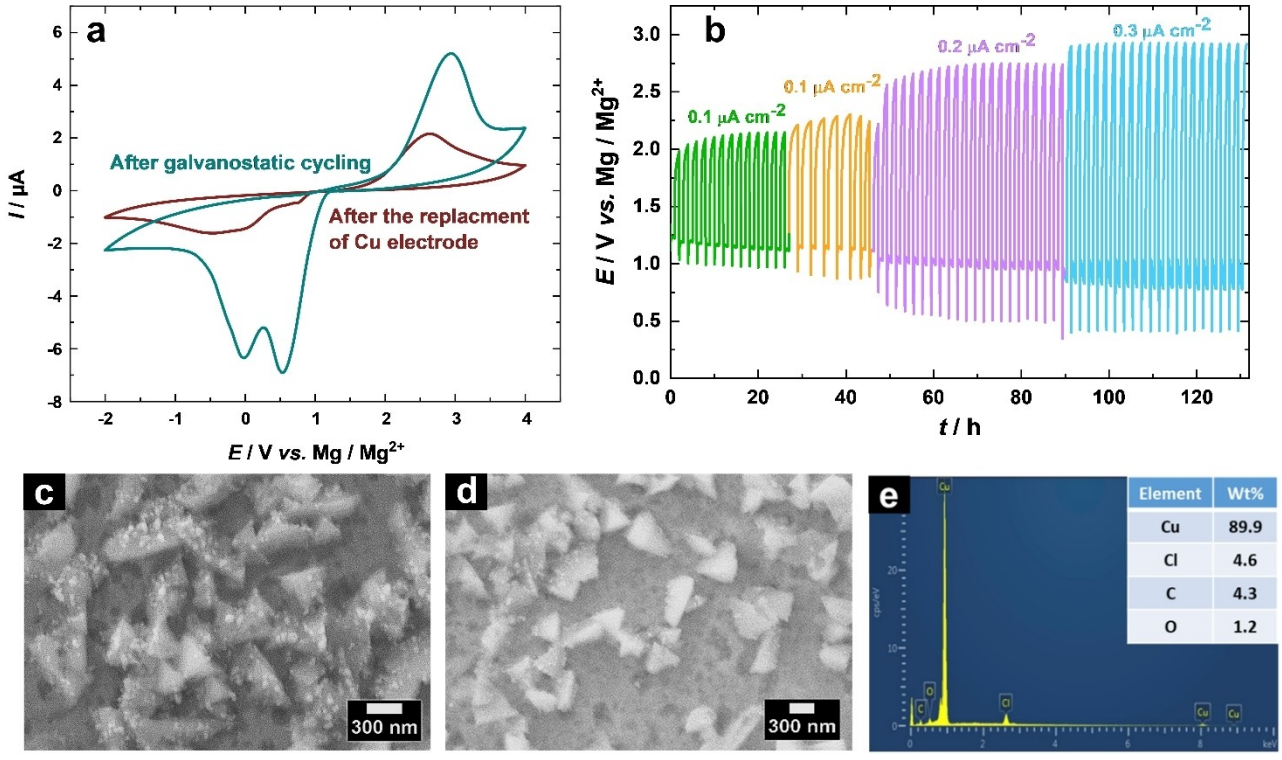

Figure 3. (a) Mg deposition–dissolution behavior on a fresh Cu electrode using a pre-used 90 %*a*-MOF1–10 %($Mg[TFSI]_2 + MgCl_2$)-G4 electrolyte and after galvanostatic cycling. Galvanostatic cycling was conducted at various current densities as depicted in (b), (c,d) SEM images, and (e) the corresponding EDS spectrum of Cu surfaces after galvanostatic cycling.

studied. In this context, the asymmetrical cell was operated at different current densities of 0.1, 0.2, and 0.3 $\mu A\,cm^{-2}$ for an overall duration of 130 h (Figure 3b). The selected current densities for the galvanostatic measurements are specifically chosen to operate in potential regimes where no Mg deposition/dissolution occurs but rather the oxidation of the Cu surface and the subsequent reduction of Cu surface oxide takes place. As such, the galvanostatic measurements focus solely on the electrochemical processes involving the Cu electrode without interference from Mg deposition. Remarkably, the amount of charge that passed significantly increases following the galvanostatic cycling measurements (Figure 3a), revealing a substantial increase in the electrochemically active surface area (EASA) due to the formation of etch pits and triangular nanoparticles, as observed in the SEM images (Figure 3c and d). The formation of etch pits implies the dissolution of Cu surfaces during the anodic treatment part of the galvanostatic cycling. Additionally, a significant amount of chloride anions (4.6 %) is detected on the Cu surfaces by EDS (Figure 3e). It appears that chloride anions are adsorbed at the electrode surface, facilitating Cu dissolution.[51,52] Furthermore, the formation of triangular nanoparticles indicates the re-deposition of Cu during the cathodic treatment.[54] To further demonstrate the role of chloride anions in Cu dissolution and thereby nanoparticle formation, a polarization experiment was conducted, employing a fresh electrolyte and fresh Cu anodes, by applying a potential of 0.4 V *vs.* Mg/Mg^{2+} for 10 h (Figure S4a). This potential value corresponds to the first cathodic peak observed in the cyclic voltammograms of Cu electrodes in the proposed semi-solid electrolyte (see Figure 2b) and is expected to be related to the re-deposition of Cu. Interestingly, after polarization at 0.4 V *vs.* Mg/Mg^{2+}, the SEM images show no particle formation and the EDS analysis demonstrates the absence of chloride anions (Figures S4b and 4c). These findings confirm that the adsorption of chloride anions at relatively high potentials induces the dissolution of the Cu surface and subsequent particle formation.

To trace these phenomena and the structural changes during the electrochemical reactions, *in-situ* EIS measurements of the Cu | 90 %*a*-MOF1–10 %($Mg[TFSI]_2 + MgCl_2$)-G4 | Mg system were conducted at various stages: at open circuit voltage (OCV = 1.1 V), at the end of Mg deposition (−0.7 μA for 20 h), and at the end of Mg dissolution (+0.7 μA for 20 h), where the lower and upper potential limits were held at −2.0 and +4.0 V, respectively (Figure 4a and b). The Nyquist plots in Figure 4a display a depressed arc at the high-frequency region and a slope (tail) at the low-frequency region. An increase in impedance is observed after Mg deposition, which correlates with an increase in polarization of the Cu electrode, resulting in higher interfacial resistance. Notably, the cell reveals an additional increase in total impedance after Cu dissolution and does not retain its initial performance, suggesting irreversible surface changes. To obtain deeper insights into the surface changes that occur after deposition and dissolution, equivalent circuit models shown in Figure 4c (models A, B, and C) have been used to fit the EIS data. Element parameters within these models were estimated using Zview software to closely match the simulated EIS spectra with the experimental data. The parameters employed for fitting the EIS results are summarized in Tables S1–S3. The equivalent circuit models consist of a series of parallel *Q*/*R* elements representing the bulk resistance and the interface. The last branch signifies the charge transfer and is composed of a constant phase element (Q_{ct}) connected in parallel with charge transfer resistance (R_{ct}) and a Warburg element (Z_w) to represent diffusion-limited kinetics, as indicated by the high-frequency tail. Moreover, we introduce an extra *Q*/*R* element to the equivalent circuit after each step (deposition and dissolution), as demonstrated in models B and C, respectively. The constant phase element (*Q*) is incorporated to account for non-ideal capacitive behavior. The origin of *Q* could be attributed to the presence of impurities in the electrochemical system and anionic electrosorption, according to the Frumkin and Melik–Gaykazyan kinetic model. This behavior is an inherent aspect of even the cleanest electrochemical systems, leading to the apparent *Q* behavior.[55]

The proposed scheme in Figure 4c can be explained as follows: The Nyquist plot at the end of the deposition process exhibits an increase in impedance at low frequency, which can be attributed to two primary factors. Firstly, it is associated with the deposition of Mg on the Cu electrode surface. Secondly, it is related to the pitting or dissolution of the Mg counter electrode. During the Mg dissolution process, the Cu electrode corrodes in the presence of chloride anions. Simultaneously, Mg is redeposited on the counter electrode, filling the pits formed during corrosion. Since the dissolution process is not 100 % reversible, few Mg deposits remain on the Cu surface. These surface changes contributed to an increase in the interfacial resistance when compared to the fresh Cu electrode at OCP. To represent these new surface changes, an additional *Q*/*R* element (Q_c and R_c) is introduced to account for the corrosion of the Cu electrode. Consequently, the total interfacial resistance is the sum of R_1, R_p, and R_f, with a value of $5.35 \cdot 10^5\ \Omega$.

Since no information about time and frequency is included in these Nyquist plots, Bode plots of Cu | 90 %*a*-MOF1–10 %($Mg[TFSI]_2 + MgCl_2$)-G4 | Mg at these three conditions are presented in Figure 4b. At all conditions, they show similar impedance in magnitude and phase shifts at the high-frequency region but diverge at the mid-high to low-frequency regions due to the change in the electrode morphology and surface area because of the redox reaction (metal deposition and dissolution). Only one broad phase maximum is observed, indicating that more than a single time constant (overlapped) is involved in the electrode processes. The characteristic variation in the phase change at the low-frequency region (100–1 Hz) is mainly used to elucidate the metal deposition where a significant decrease in the phase shift is observed due to the growth of deposits.

On the other hand, we extended our study to explore possible changes in the developed semi-solid electrolyte following the previous galvanostatic cycling (refer to Figure 3b) and after applying higher current densities of ±0.5 and 1.0 $\mu A\,cm^{-2}$ (Mg deposition–dissolution regime) (Figure S5). Notably, both the surface morphology and the chemical composition are altered after galvanostatic cycling in both regimes, as demonstrated by SEM images and EDS-mapping

Research Article
doi.org/10.1002/batt.202400420
Chemistry Europe
European Chemical Societies Publishing

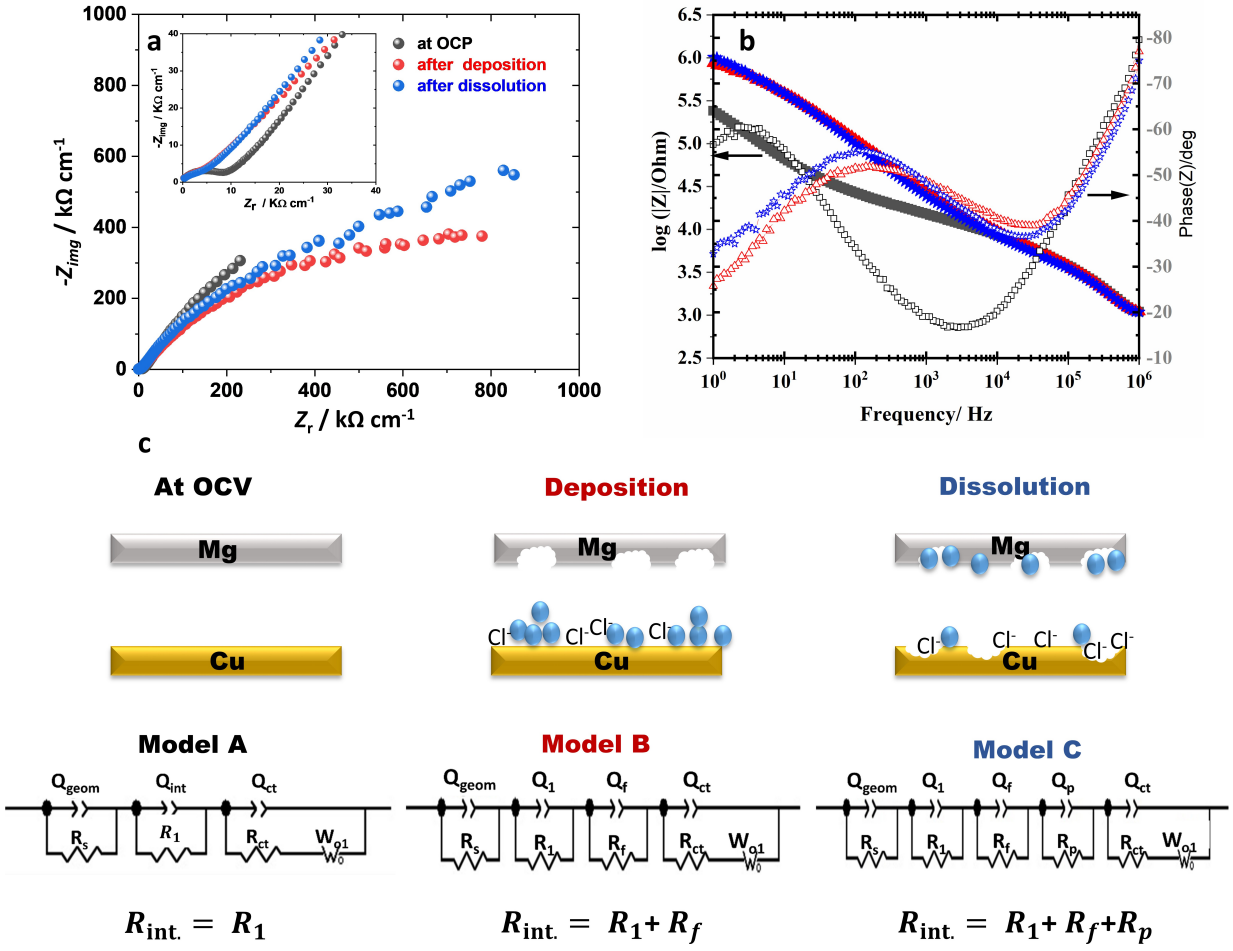

Figure 4. (a) Nyquist plots and (b) Bode plots illustrating the electrochemical behavior of the Cu | 90 %*a*-MOF1–10 %(Mg[TFSI]$_2$ + MgCl$_2$)-G4 | Mg system. (c) Schematic representation and corresponding models depicting the electrochemical processes occurring at the Cu working electrode and Mg counter electrode under open circuit potential (OCP), during deposition, and dissolution stages.

analysis, respectively (Figure 5a–f). The particles become more agglomerated accompanied by the presence of a significant amount of Cu ions (5.8 wt %) after galvanostatic cycling up to ±0.3 μA cm^{-2} (Figure 5c and d), compared to the as-synthesized semi-solid electrolyte (Figure 5a and b). This can be attributed to the dissolution of the Cu anode. In comparison, expanding the galvanostatic cycling to higher current densities of ±0.5 and ±1.0 μA cm^{-2}, more significant morphological changes in the semi-solid electrolyte are observed. The electrolyte undergoes a transition towards increased crystallinity, characterized by the emergence of well-defined microcrystals (Figure 5e), indicative of Mgbp3dc recrystallization, as corroborated by the XRD pattern (Figure S6). Furthermore, the electrolyte contains Cu ions (4.8 wt %) (Figure 5f), suggesting that dissolved Cu ions may catalyze MOF recrystallization under relatively high current densities, facilitating the formation of these microcrystals.

An XPS analysis was also conducted to identify alterations in the chemical composition of the semi-solid electrolyte after the galvanostatic cycling in the Mg deposition–dissolution regime. Upon comparison with the XPS spectrum of the fresh electrolyte, the XPS analysis after galvanostatic cycling reveals the appearance of Cu-2*p* signals (Figure 6a and b). The high-resolution spectrum of Cu-2*p* can be deconvoluted into Cu-2$p_{1/2}$ and Cu-2$p_{3/2}$, with the presence of a satellite peak observed at 943.9 eV. The Cu-2$p_{1/2}$ signal can be further deconvoluted into two peaks at 953.3 and 951.4 eV, corresponding to Cu(II) and Cu(I) states, respectively. Similarly, the Cu-2$p_{3/2}$ signal exhibits two peaks at 936.3 and 932.3 eV, attributed to Cu(II) and Cu(I) states, respectively. Additionally, the satellite peak at around 943.5 eV arise from shake-ups of the 3*d* (9) states of Cu(II).[56] The high-resolution XPS spectrum of Cl-2*p* indicates the formation of Cu(I)Cl as a corrosion product of the Cu anode during the galvanostatic cycling, as depicted in Figure 5a and b.[57]

3. Conclusions

Our investigation delves into the impact of chloride ions on Mg deposition/dissolution processes on Cu electrodes using a semi-solid electrolyte with a low solvent content (15–20 %), composed of a blend of MOFs including *a*-Mg(bp3dc) and *α*-Mg$_3$(HCOO)$_6$ along with MgCl$_2$ and Mg[TFSI]$_2$. We highlighted the crucial role of chloride ions in enhancing Mg dissolution on

Research Article
doi.org/10.1002/batt.202400420
Chemistry Europe
European Chemical Societies Publishing

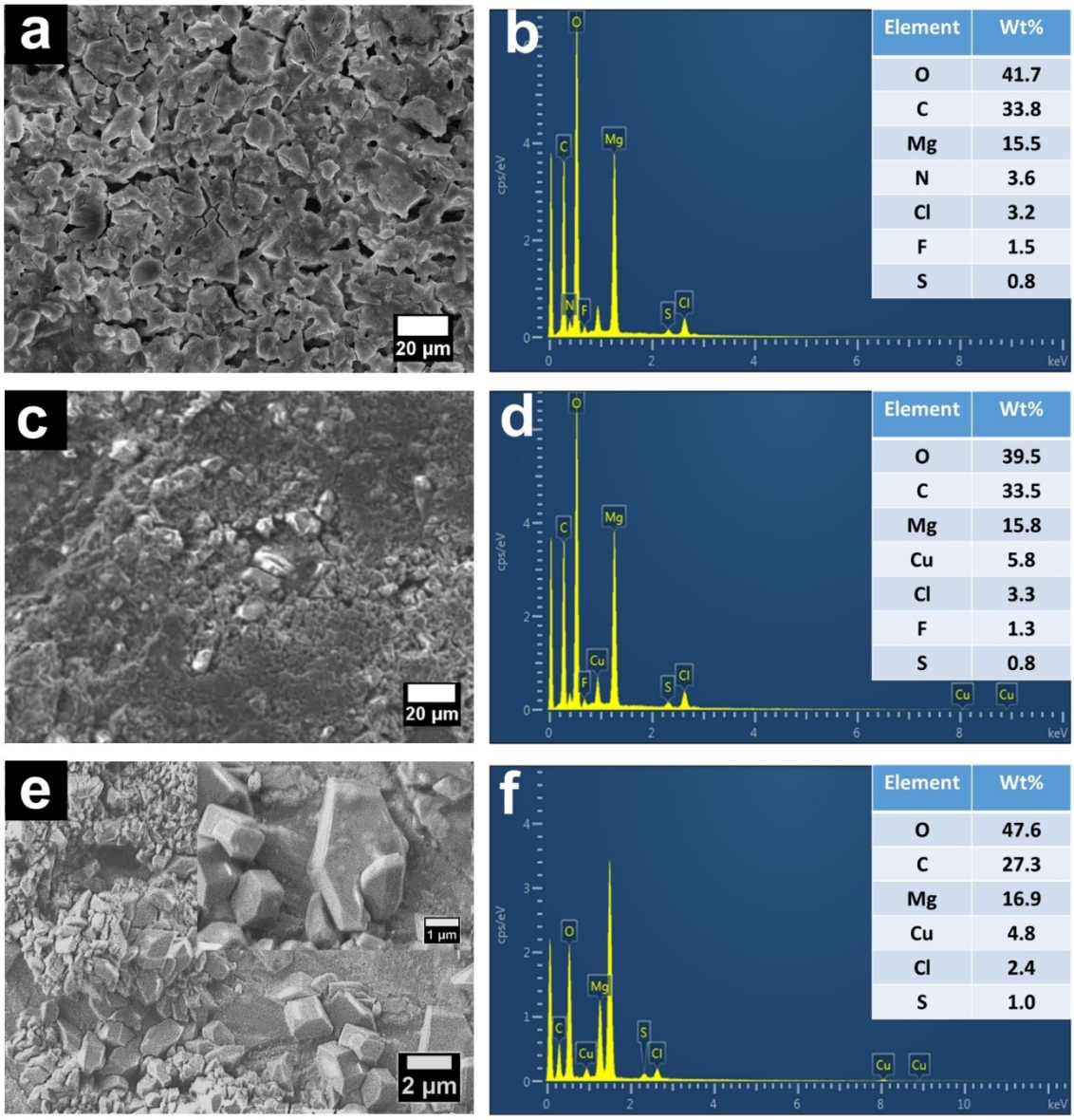

Figure 5. SEM images and corresponding EDS spectra of (a, b) the as-synthesized semi-solid electrolyte and after galvanostatic cycling (c, d) at low current densities where no Mg deposition occurs, and (e, f) at high current densities within the Mg deposition-dissolution region.

Cu electrodes. Extending the upper potential limit to 4.0 V *vs.* Mg/Mg^{2+} intensified Mg dissolution. The chloride ions present in the semi-solid electrolyte facilitate Cu surface dissolution thereby providing new active sites for further Mg deposition. Morphological and compositional analyses after cycling reveal pitting corrosion, indicating the corrosive nature of chloride-containing semi-solid electrolytes, akin to liquid electrolytes. Galvanostatic measurements show oxidation of the Cu surface and subsequent reduction of Cu surface oxide, forming triangular nanoparticles. Chloride anions adsorbed at the electrode surface trigger Cu dissolution followed by re-deposition during cathodic treatment, resulting in nanoparticle formation. Structural changes during Mg deposition/dissolution are analyzed using *in-situ* electrochemical impedance spectroscopy (EIS) and equivalent circuit models, providing insights into the interfacial behavior. Moreover, the semi-solid electrolyte based on MOFs demonstrates stability and retains the performance after repeated cycling, indicating its potential for practical Mg-ion battery applications despite the high Mg overpotential observed in this study, which can be further optimized. In our recent work,[46] we explored the factors affecting Mg overpotential, showing that adjustments to various components of the MOF-based semi-solid electrolyte—such as MOF structure and activation, guest solvent, and the nature and composition of the Mg salt—can have a significant impact on reducing the Mg overpotential.

Research Article
doi.org/10.1002/batt.202400420
Chemistry Europe
European Chemical Societies Publishing

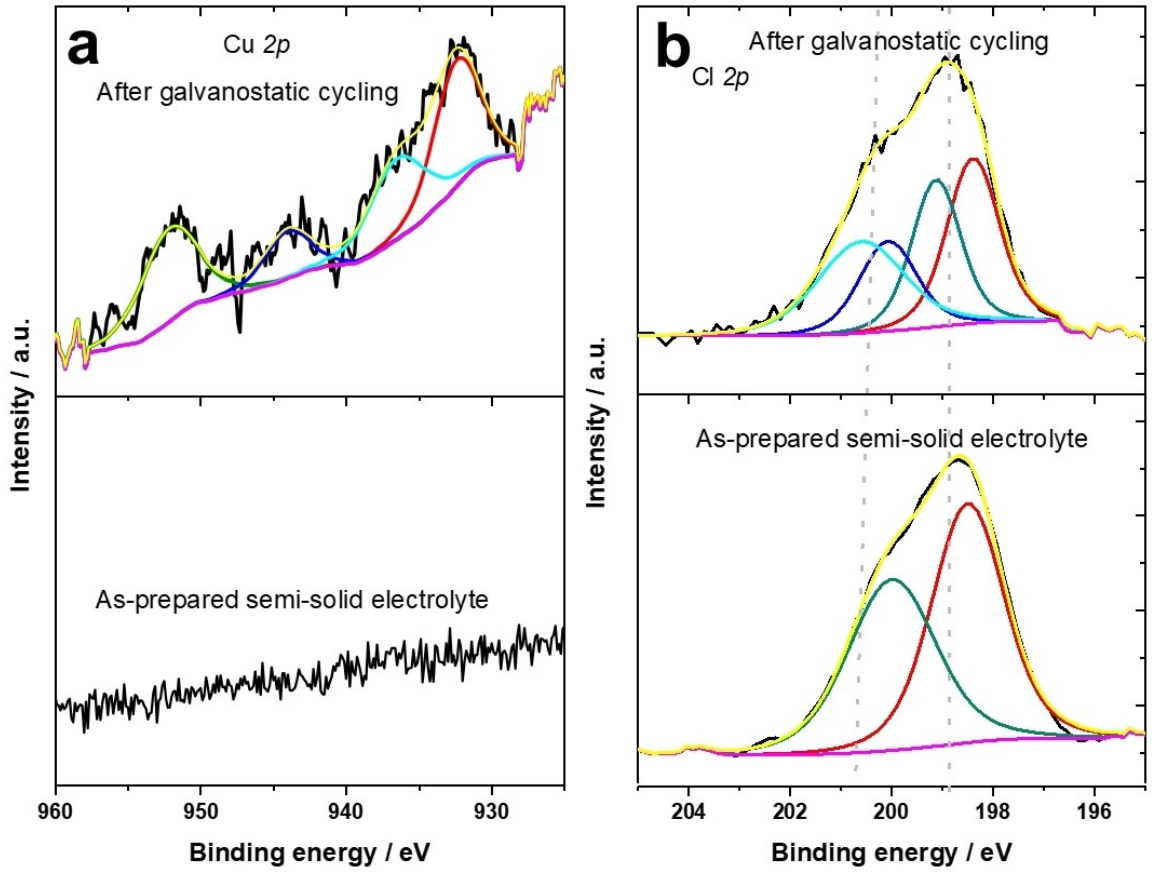

Figure 6. X-ray photoelectron spectra of (a) core level Cu-2*p* and (b) core level Cl-2*p* of the as-prepared semi-solid electrolyte and after galvanostatic cycling in the Mg deposition-dissolution regime.

Acknowledgements

The authors gratefully acknowledge funding by the DFG (Deutsche Forschungsgemeinschaft) through research unit FOR-5065 (id 428906592) and project 501805371 as well as by the BMBF (Bundesministerium fur Bildung und Forschung) through the project CASINO (FKZ: 03XP0487G) and the state of Baden-Württemberg and the DFG through grant no INST 40/574-1 FUGG. Open Access funding enabled and organized by Projekt DEAL.

Conflict of Interests

The authors declare no conflict of interest.

Data Availability Statement

All data are available for sharing based on the DFG's Code of Conduct "Safeguarding Good Research Practice".

Keywords: Metal-organic frameworks · Semi-solid electrolytes · Mg batteries · Chloride ions · Cu corrosion

[1] Y. Liang, H. Dong, D. Aurbach, Y. Yao, *Nat. Energy* **2020**, *5*, 646–656. DOI: https://doi.org/10.1038/s41560-020-0655-0.
[2] J. W. Choi, D. Aurbach, *Nat. Rev. Mater.* **2016**, *1*, 16013. DOI: https://doi.org/10.1038/natrevmats.2016.13.
[3] K. W. Leong, W. Pan, X. Yi, S. Luo, X. Zhao, Y. Zhang, Y. Wang, J. Mao, Y. Chen, J. Xuan, H. Wang, D. Y. C. Leung, *Sci. Adv.* **2023**, *9*. DOI: https://doi.org/10.1126/sciadv.adh1181.
[4] I. Huang, Y. Zhang, H. M. Arafa, S. Li, A. Vazquez-Guardado, W. Ouyang, F. Liu, S. Madhvapathy, J. W. Song, A. Tzavelis, J. Trueb, Y. Choi, W. J. Jeang, V. Forsberg, E. Higbee-Dempsey, N. Ghoreishi-Haack, I. Stepien, K. Bailey, S. Han, Z. J. Zhang, C. Good, Y. Huang, A. J. Bandodkar, J. A. Rogers, *Energy Environ. Sci.* **2022**, *15*, 4095–4108. DOI: https://doi.org/10.1039/D2EE01966C.
[5] W. Zhang, Q. Zhao, Y. Hou, Z. Shen, L. Fan, S. Zhou, Y. Lu, L. A. Archer, *Sci. Adv.* **2021**, *7*, eabl3752. DOI: https://doi.org/10.1126/sciadv.abl3752.
[6] H. Tian, T. Gao, X. Li, X. Wang, C. Luo, X. Fan, C. Yang, L. Suo, Z. Ma, W. Han, C. Wang, *Nat. Commun.* **2017**, *8*, 14083. DOI: https://doi.org/10.1038/ncomms14083.
[7] H. D. Yoo, S.-D. Han, I. L. Bolotin, G. M. Nolis, R. D. Bayliss, A. K. Burrell, J. T. Vaughey, J. Cabana, *Langmuir* **2017**, *33*, 9398–9406. DOI: https://doi.org/10.1021/acs.langmuir.7b01051.
[8] R. Deivanayagam, B. J. Ingram, R. Shahbazian-Yassar, *Energy Storage Mater.* **2019**, *21*, 136–153. DOI: https://doi.org/10.1016/j.ensm.2019.05.028.
[9] Y. Man, P. Jaumaux, Y. Xu, Y. Fei, X. Mo, G. Wang, X. Zhou, *Sci. Bull. (Beijing).* **2023**, *68*, 1819–1842. DOI: https://doi.org/10.1016/j.scib.2023.07.027.
[10] J. Muldoon, C. B. Bucur, A. G. Oliver, T. Sugimoto, M. Matsui, H. S. Kim, G. D. Allred, J. Zajicek, Y. Kotani, *Energy Environ. Sci.* **2012**, *5*, 5941. DOI: https://doi.org/10.1039/c2ee03029b.
[11] H. Zhang, L. Qiao, H. Kühnle, E. Figgemeier, M. Armand, G. G. Eshetu, *Energy Environ. Sci.* **2023**, *16*, 11–52. DOI: https://doi.org/10.1039/D2EE02998G.

[12] J. Luo, S. He, T. L. Liu, *ACS Energy Lett.* **2017**, *2*, 1197–1202. DOI: https://doi.org/10.1021/acsenergylett.7b00269.
[13] J. Luo, Y. Bi, L. Zhang, X. Zhang, T. L. Liu, A Stable, *Angew. Chem. Int. Edition* **2019**, *58*, 6967–6971. DOI: https://doi.org/10.1002/anie.201902009.
[14] B. Pan, J. Huang, M. He, S. M. Brombosz, J. T. Vaughey, L. Zhang, A. K. Burrell, Z. Zhang, C. Liao, *ChemSusChem* **2016**, *9*, 595–599. DOI: https://doi.org/10.1002/cssc.201501557.
[15] G. Bieker, M. Salama, M. Kolek, Y. Gofer, P. Bieker, D. Aurbach, M. Winter, *ACS Appl. Mater. Interfaces* **2019**, *11*, 24057–24066. DOI: https://doi.org/10.1021/acsami.9b05307.
[16] H. Zhang, L. Qiao, M. Armand, *Angew. Chem. Int. Edition* **2022** *61*. DOI: https://doi.org/10.1002/anie.202214054.
[17] R. Attias, M. Salama, B. Hirsch, Y. Goffer, D. Aurbach, *Joule* **2019**, *3*, 27–52. DOI: https://doi.org/10.1016/j.joule.2018.10.028.
[18] J. G. Connell, B. Genorio, P. P. Lopes, D. Strmcnik, V. R. Stamenkovic, N. M. Markovic, *Chem. Mater.* **2016**, *28*, 8268–8277. DOI: https://doi.org/10.1021/acs.chemmater.6b03227.
[19] D.-T. Nguyen, A. Y. S. Eng, R. Horia, Z. Sofer, A. D. Handoko, M.-F. Ng, Z. W. Seh, *Energy Storage Mater.* **2022**, *45*, 1120–1132. DOI: https://doi.org/10.1016/j.ensm.2021.11.011.
[20] N. Sa, B. Pan, A. Saha-Shah, A. A. Hubaud, J. T. Vaughey, L. A. Baker, C. Liao, A. K. Burrell, *ACS Appl. Mater. Interfaces* **2016**, *8*, 16002–16008. DOI: https://doi.org/10.1021/acsami.6b03193.
[21] D.-T. Nguyen, A. Y. S. Eng, M.-F. Ng, V. Kumar, Z. Sofer, A. D. Handoko, G. S. Subramanian, Z. W. She, *Cell Rep. Phys. Sci.* **2020**, 1100265. DOI: https://doi.org/10.1016/j.xcrp.2020.100265.
[22] R. Attias, M. S. Chae, B. Dlugatch, M. Oliel, Y. Goffer, D. Aurbach, *ACS Catal.* **2020**, *10*, 7773–7784. DOI: https://doi.org/10.1021/acscatal.0c01956.
[23] J. G. Connell, B. Genorio, P. P. Lopes, D. Strmcnik, V. R. Stamenkovic, N. M. Markovic, *Chem. Mater.* **2016**, *28*, 8268–8277. DOI: https://doi.org/10.1021/acs.chemmater.6b03227.
[24] J. Muldoon, C. B. Bucur, A. G. Oliver, J. Zajicek, G. D. Allred, W. C. Boggess, *Energy Environ. Sci.* **2013**, *6*, 482–487. DOI: https://doi.org/10.1039/C2EE23686A.
[25] T. W. Cain, I. Gonzalez-Afanador, N. Birbilis, J. R. Scully, *J. Electrochem. Soc.* **2017**, *164*, C300–C311. DOI: https://doi.org/10.1149/2.1371706jes..
[26] Y. Li, S. Guan, H. Huo, Y. Ma, Y. Gao, P. Zuo, G. Yin, *Adv. Funct. Mater.* **2021**, *31*, 2100650. DOI: https://doi.org/10.1002/adfm.20210065031.
[27] Z. Zhao-Karger, R. Liu, W. Dai, Z. Li, T. Diemant, B. P. Vinayan, C. Bonatto Minella, X. Yu, A. Manthiram, R. J. Behm, M. Ruben, M. Fichtner, *ACS Energy Lett.* **2018**, *3*, 2005–2013. DOI: https://doi.org/10.1021/acsenergylett.8b01061.
[28] Z. Zhao-Karger, M. E. Gil Bardaji, O. Fuhr, M. Fichtner, *Chem. A Mater.* **2017**, *5*, 10815–10820. DOI: https://doi.org/10.1039/C7TA02237A.
[29] Z. Zhao-Karger, R. Liu, W. Dai, Z. Li, T. Diemant, B. P. Vinayan, C. Bonatto Minella, X. Yu, A. Manthiram, R. J. Behm, M. Ruben, M. Fichtner, *ACS Energy Lett.* **2018**, *3*, 2005–2013. DOI: https://doi.org/10.1021/acsenergylett.8b01061.
[30] W. Ren, M. Cheng, Y. Wang, D. Zhang, Y. Yang, J. Yang, J. Wang, *Batter Supercaps* **2022**, *5*, e202200263. DOI: https://doi.org/10.1002/batt.202200263.
[31] O. Tutusaus, R. Mohtadi, T. S. Arthur, F. Mizuno, E. G. Nelson, Y. V. Sevryugina, *Angew. Chem. Int. Ed.* **2015**, *54*, 7900–7904. DOI: https://doi.org/10.1002/anie.201412202.
[32] D. Chinnadurai, Y. Li, C. Zhang, G. Yang, W. Y. Lieu, S. Kumar, Z. Xing, W. Liu, Z. W. Seh, *Nano Lett.* **2023**, *23*, 11233–11242. DOI: https://doi.org/10.1021/acs.nanolett.3c03740.
[33] M. Cheng, W. Ren, D. Zhang, S. Zhang, Y. Yang, X. Lv, J. Yang, J. Wang, *Energy Storage Mater.* **2022**, *51*, 764–77. DOI: https://doi.org/10.1016/j.ensm.2022.07.021.
[34] Y. Man, P. Jaumaux, Y. Xu, Y. Fei, X. Mo, G. Wang, X. Zhou, *Sci. Bull. (Beijing)* **2023**, *68*, 1819–1842. DOI: https://doi.org/10.1016/j.scib.2023.07.027.
[35] S.-Y. Ha, Y.-W. Lee, S. W. Woo, B. Koo, J.-S. Kim, J. Cho, K. T. Lee, N.-S. Choi, *ACS Appl. Mater. Interfaces* **2014**, *6*, 4063–4073. DOI: https://doi.org/10.1021/am405619v.
[36] Q. Wu, K. Shu, L. Sun, H. Wang, *Front. Mater.* **2021**, *7*. DOI: https://doi.org/10.3389/fmats.2020.612134.
[37] R. Zhang, C. Cui, R. Li, Y. Li, C. Du, Y. Gao, H. Huo, Y. Ma, P. Zuo, G. Yin, *Chem. Eng. J.* **2021**, *426*, 130751. DOI: https://doi.org/10.1016/j.cej.2021.130751.
[38] E. N. Keyzer, H. F. J. Glass, Z. Liu, P. M. Bayley, S. E. Dutton, C. P. Grey, D. S. Wright, *J. Am. Chem. Soc.* **2016**, *138*, 8682–8685. DOI: https://doi.org/10.1021/jacs.6b04319.
[39] J. Lu, P. Jaumaux, T. Wang, C. Wang, G. Wang, *Chem. A Mater.* **2021**, *9*, 24175–24194. DOI: https://doi.org/10.1039/D1TA06606D.
[40] P. A. Helen, P. C. Selvin, P. Sakthivel, *J. Solid State Electrochem.* **2024**. DOI: https://doi.org/10.1007/s10008-024-05867-w.
[41] T. Wang, X. Zhao, F. Liu, L.-Z. Fan, *J. Energy Chem.* **2021**, *59*, 608–614. DOI: https://doi.org/10.1016/j.jechem.2020.12.004.
[42] J. Sun, Y. Zou, S. Gao, L. Shao, C. Chen, *ACS Appl. Mater. Interfaces* **2020**, *12*, 54711–54719. DOI: https://doi.org/10.1021/acsami.0c16204.
[43] H. Shuai, J. Xu, K. Huang, *Coord. Chem. Rev.* **2020**, *422*, 213478. DOI: https://doi.org/10.1016/j.ccr.2020.213478.
[44] M. Guo, C. Yuan, T. Zhang, X. Yu, *Small*, **2022**, *18*, 2106981. DOI: https://doi.org/10.1002/smll.202106981.
[45] P. Seggem, V. R. Jetti, P. Basak, *Energy Mater.* **2022**, *5*, 6606–6617. DOI: https://doi.org/10.1021/acsaem.1c04057.
[46] H. K. Hassan, P. Hoffmann, T. Jacob, *ChemSusChem* **2024**, *17*, e202301362. DOI: https://doi.org/10.1002/cssc.202301362.
[47] E. M. Miner, S. S. Park, M. Dincă, *J. Am. Chem. Soc.* **2019**, *141*, 4422–4427. DOI: https://doi.org/10.1021/jacs.8b13418.
[48] X. Hu, Q. Liu, K. Lin, C. Han, B. Li, *Chem. A. Mater.* **2021**, *9*, 20837–20856. DOI: https://doi.org/10.1039/D1TA05201B.
[49] M. L. Aubrey, R. Ameloot, B. M. Wiers, J. R. Long, *Energy Environ. Sci.* **2014**, *7*, 667. DOI: https://doi.org/10.1039/c3ee43143^f.
[50] H. K. Hassan, A. Farkas, A. Varzi, T. Jacob, *Batter Supercaps* **2022**, *5*, e202200260. DOI: https://doi.org/10.1002/batt.202200260.
[51] T. A. Green, P. Valverde, S. Roy, *J. Electrochem. Soc.* **2018**, *165*, D313–D320. DOI: https://doi.org/10.1149/2.0371809jes.
[52] Y. Cheng, T. Liu, Y. Shao, M. H. Engelhard, J. Liu, G. Li, *J. Mater. Chem. A* **2014**, *2*, 2473–2477. DOI: https://doi.org/10.1039/C3TA15113A.
[53] R. Dominko, J. Bitenc, R. Berthelot, M. Gauthier, G. Pagot, V. Di Noto, *J. Power Sources* **2020**, *478* 229027. . DOI: https://doi.org/10.1016/j.jpowsour.2020.229027.
[54] M. M. Elnagar, L. A. Kibler, T. Jacob, *J. Electrochem. Soc.* **2022**, *169*, 102509. DOI: https://doi.org/10.1149/1945-7111/ac9930.
[55] A. Lasia, *J. Phys. Chem. Lett.* **2022**, *13*, 580–589. DOI: https://doi.org/10.1021/acs.jpclett.1c03782.
[56] N. Pauly, S. Tougaard, F. Yubero, *Surf. Sci.* **2014**, *620*, 17–22 DOI: https://doi.org/10.1016/j.susc.2013.10.009.
[57] B. Liu, J. Liu, Y. Liu, S. Gong, Y. Dai, G. Zhao, G. Xie, L. Peng, Z. Li, *Mater. Charact.* **2020**, *167*, 110476. DOI: https://doi.org/10.1016/j.matchar.2020.110476.

Manuscript received: June 26, 2024
Revised manuscript received: September 4, 2024
Accepted manuscript online: September 18, 2024
Version of record online: ■■, ■■

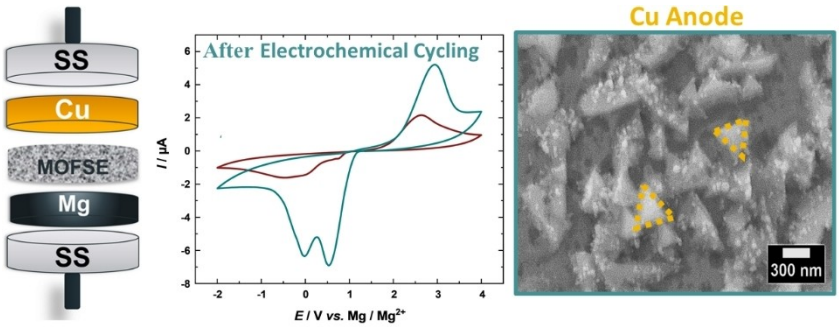

Chloride anions in the semi-solid electrolyte adsorb onto the electrode surface, triggering Cu dissolution followed by re-deposition during cathodic treatment. This results in the formation of triangular nanoparticles and a significant increase in the electrochemically active surface area, providing new active sites for additional Mg deposition.

M. M. Elnagar, H. K. Hassan, L. A. Kibler, T. Jacob**

1 – 11

Effect of Chloride Ions on the Electrochemical Performance of Magnesium Metal-Organic-Frameworks-Based Semi-Solid Electrolytes